Master of Science thesis in Complex Adaptive Systems

Method development and pilot experiments for the R^3B micro-vertex tracker

JULIUS HAGDAHL

Chalmers University of Technology
Department of Fundamental Physics

Göteborg, 2011

Method development and pilot experiments for the R^3B micro-vertex tracker
JULIUS HAGDAHL

Department of Fundamental Physics
Chalmers University of Technology

SE-412 96 Göteborg
Sweden
Telephone + 46 (0)31-772 1000

Cover: Template cluster shapes for DSSSD events with varying η-values.
See page 38 for further details.

Göteborg, Sweden 2011

Abstract

Radioactive beam experiments allow physicists to study nuclei at the limits of stability. Knowledge about the properties of such exotic nuclei is essential for understanding the processes of stellar nucleosynthesis through which all elements heavier than hydrogen are formed.

The LAND experimental setup at the GSI facility outside Darmstadt, Germany, can measure properties of highly unstable nuclei using invariant mass reconstruction. One of the key detector systems of this setup is the micro-vertex tracker; an array of double-sided silicon strip detectors used for energy loss and position measurements. This thesis aims to give an introduction to the properties of these detectors and the methods used for calibrating and analysing the measurement data they produce. Furthermore, an alternative approach to analysing the measurement data is described and evaluated. This approach aims to extract physical quantities from the detector signals by matching them to sets of characteristic templates for different types of events.

Such templates have been calculated from data acquired during the S393 experiment which was carried out in the fall of 2010. An attempt to reconstruct properties of these events based on these clusters was then performed.

It was found to be difficult to calculate templates for the different event characteristics with small enough errors to be able to successfully reconstruct events using this method. Although the overall performance of this alternative method was found to be disappointing, the results presented can hopefully provide a basis for further development.

Also included is a brief description of an alternative unpacker software which implements a reduced data format for the micro-vertex tracker. This format aims to reduce the amount of data produced by the detector system through a non-feature removal algorithm, allowing it to identify and discard all non-significant signals from the tracker.

Contents

1 Introduction **1**

1.1 Purpose and scope 1

1.2 Outline 2

2 Background **3**

2.1 Exotic nuclei 3

2.2 Radioactive beams 3

2.3 GSI and the LAND-setup 4

2.3.1 The LAND-setup 5

2.3.2 FAIR and R^3B 6

2.3.3 The S393 experiment 7

3 Silicon microstrip detectors **9**

3.1 Semiconductors 9

3.1.1 Doping and *pn*-junctions 10

3.2 Semiconductors as detectors 11

3.2.1 Silicon microstrip detectors 13

4 The micro-vertex tracker **17**

4.1 Overview 17

4.2 Front-end electronics and readout 18

4.3 Unpacking 19

4.3.1 The *land02* unpacker 19

4.3.2 Data formats 19

5 Analysis and calibration **23**

5.1 Basic concepts 23

5.1.1 Signal components 23

5.1.2 Energy loss 24

5.1.3 Hit position 24

5.1.4 Corrections 25

5.1.5 Dead strips 29

5.2 Cluster fitting 30

5.2.1 Template clusters 31

6 Results **33**

6.1 Template clusters 33

6.1.1 Basic behaviour 33

6.1.2 Identification of bad stretches 35

6.1.3 Centering 35

6.1.4 Calculated template clusters 38

6.1.5 η-reconstruction 41

7 Conclusion and outlook **43**

References **45**

A Glossary **47**

1. Introduction

The aim of nuclear physics is to describe and understand the properties of atomic nuclei. Although the nuclei are built up from only two simple constituents, the proton and the neutron, interacting through the strong, weak and electromagnetic force[1], nuclei themselves exhibit a wide range of properties. As such, they are a fine example of complexity emerging from seemingly simple parts. Approximated and simplified models have proven highly successful for describing the structure and properties of stable nuclei, but for nuclei far away from the "valley of stability", these models lose their validity. Such nuclei are, however, important for the understanding of stellar nucleosynthesis, the processes through which all heavier elements are formed.

During the last decades, nuclear research using radioactive beams has seen a steadily increasing interest. New facilities that are able to deliver intense beams of exotic nuclear species, combined with state-of-the-art instrumentation, allow physicists to study systems with extreme isospin near, and beyond, the neutron and proton driplines, the very limits of nuclear stability. Such experiments require not only great theoretical knowledge within the field of nuclear physics itself, but also a great amount of engineering expertise.

The Subatomic Physics group at Chalmers University of Technology is deeply involved in the R^3B project at the future FAIR facility in Darmstadt, Germany. This project aims to design and implement a state-of-the-art experimental setup for studying nuclear reactions at relativistic energies with kinematically complete measurements. One of the key detector subsystems of this experimental setup is the micro-vertex tracker for charged particles. It is formed by an array of double-sided silicon strip detectors (DSSSDs). A prototype system is in operation at the LAND-setup, the experimental setup which is currently evolving into R^3B.

1.1 Purpose and scope

This master thesis project is aimed at studying calibration and identification methods for the R^3B micro-vertex tracker. The analysis of data produced by the prototype system at the LAND-setup during the S393 experiment forms the basis of this work.

More specifically, the prospect of creating a set of templates for the behavior of the signals of the DSSSD detectors depending on the position and energy of the

[1] Gravity can be neglected at such small scales.

hit is studied. Such a set of templates could then be used to reconstruct events in the detector, including events which cannot be easily handled with currently implemented methods.

1.2 Outline

The first section of this thesis aims to give a brief introduction to the field of experimental nuclear physics, with a focus on exotic nuclei research using radioactive beams. Also, a short overview of the GSI facility and the LAND setup, as well as the planned FAIR facility and R^3B setup is provided. Finally, the S393 experiment is briefly presented.

Following this is an short overview of semiconductor detectors in general, as well as a somewhat more extensive background on silicon microstrip detectors. The thesis then moves on to the specific silicon microstrip detector system in place at the LAND-setup, the micro-vertex tracker prototype. The basic principles of calibration and analysis of the data from this detector system is discussed before moving on to the alternative analysis method investigated during this thesis work.

Brief explanations of acronyms and technical terms are given in the appended glossary.

2. Background

2.1 Exotic nuclei

The *shell model*, which was developed in the late 1940s, is still commonly used for describing the properties and structure of atomic nuclei[1]. In this model, protons and neutrons are treated as quantum-mechanical fermions, occupying orbits similar to atomic electrons, and being confined by a common potential. These assumptions and approximations still allow the shell model to capture most properties of stable nuclei. For instance, nuclei with "magic" proton and neutron numbers associated with full proton and neutron shells have been shown experimentally to be more stable against nuclear decay [1].

Unfortunately, the assumptions and approximations made in this model become decreasingly valid when moving away from stability through the addition of extra protons or neutrons. As one approaches the neutron or proton driplines, predicted magic numbers may no longer coincide with the most stable nuclear configurations, and new exotic nuclear structures are observed.

An example of the structural peculiarities found among light exotic nuclei at the driplines are so-called *halo nuclei*. They consist of one or two weakly bound nucleons "orbiting" a tightly bound core at a large, classically forbidden, distance. Such nuclei, with two loosely bound nucleons, are often likened to the Borromean rings in that the whole system falls apart if one component is removed. Another, hypothetical, example is the tetra-neutron, a stable cluster formed by four neutrons.

2.2 Radioactive beams

Nuclear reactions are usually studied by accelerating some simple projectile, such as a single proton, and colliding it with a target made up of heavier nuclei. Such experiments are, however, not possible if the heavy nuclei in question are highly unstable. As isotopes near the driplines may have lifetimes of only tiny fractions of a second, making a target out of these nuclei is not a viable option.

The solution to this problem is to instead make the beam out of the exotic ions,

[1]Naturally, there have been improvements made to the model, but the basic principles have remained intact.

which are produced in some other nuclear reaction, and impinge it on a target made from simple particles. Of course, one cannot make a target out of, e.g., "pure" protons. Rather, in the case of protons, one would make the target out of hydrogen, or hydrogen-rich molecules. Experiments of this type, where the target and projectile are interchanged, are referred to as inverse kinematics experiments.

2.3 GSI and the LAND-setup

GSI is a heavy-ion research facility outside Darmstadt, Germany. The accelerators at the facility are capable of producing beams of stable ions up to ^{238}U, with beam energies in the range of a few GeV [2]. A schematic overview of the facility is presented in figure 2.1.

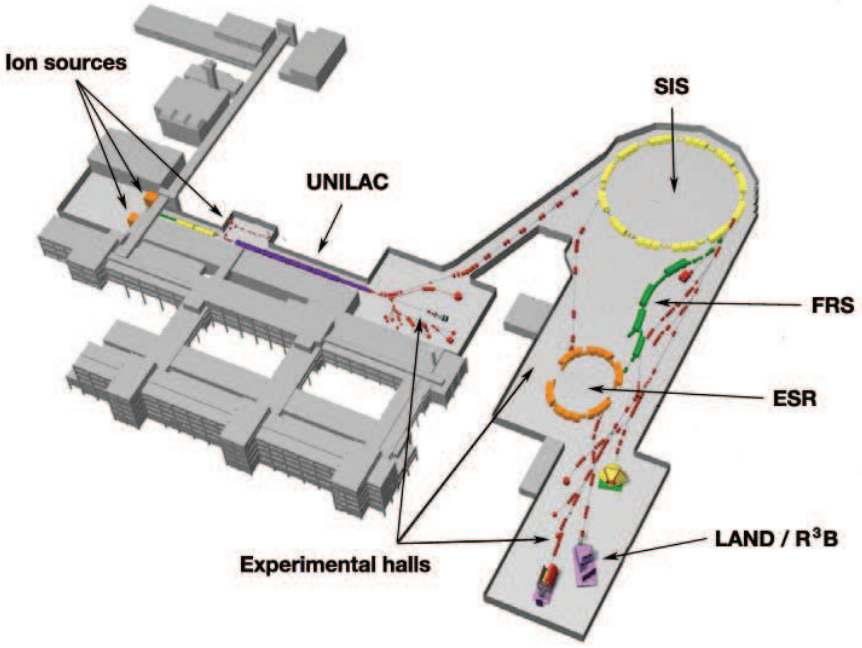

Figure 2.1: Overview of the GSI facility. Original picture from [3]

The UNILAC (UNIversal Linear ACcelerator) accelerates ions from one of three ion sources to energies up to 11.4 MeV/u. The beam can then be used directly for low-energy experiments, or it can be injected into the SIS (SchwerIonen Synchrotron) for further acceleration. The high-energy beam of stable isotopes from the SIS may then be used directly in experiments or to produce a radioactive beam of unstable isotopes through the FRS (FRagment Separator).

The radioactive beam is produced by impinging the primary beam from the SIS on a production target. Through fragmentation reactions a secondary beam consisting

of a wide range of isotopes[2] is produced. By passing the secondary beam through the FRS, which consists of a series of dipole magnets and degraders, single isotopes can be selected for transmission to the experimental caves based on their charge and charge-to-mass ratio.

2.3.1 The LAND-setup

The LAND-setup, shown in figure 2.2, is designed for studying nuclear reactions with radioactive or stable ions at relativistic energies. This is done through kinematically complete measurements, i.e., by measuring the momenta and species of all particles before and after the reaction. This allows for invariant mass reconstruction, which in turn can provide information on the states of the reacting nuclei. An overview of the LAND-setup is shown in figure 2.2. The incoming beam from the FRS first arrives at the POS, a plastic scintillator used for beam position and time measurements, before reaching the ROLU. The ROLU consists of four scintillators mounted so that they can be moved in and out of the beam, forming a rectangular aperture. By using the trigger from these scintillators as a veto, it can essentially be used to control the emittance of the beam[3].

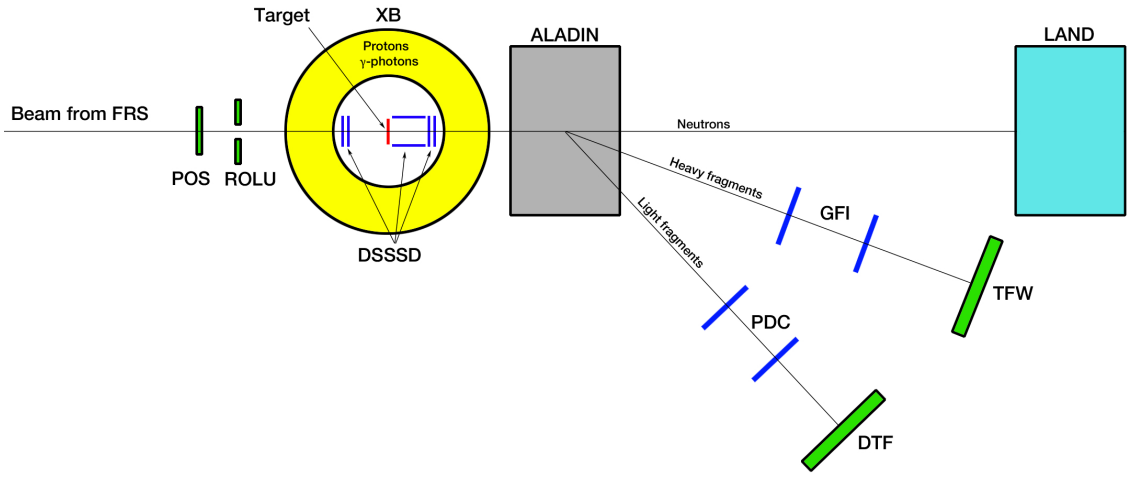

Figure 2.2: A schematic view of the LAND-setup. The beam enters from the left and reacts with the target inside the XB. Outgoing fragments at small angles with regards to the beam line are deflected to different angles depending on their charges and momenta by the ALADiN dipole.

The target, which sits inside a vacuum chamber, is surrounded by two detector

[2]Its exact composition depends on the energy and species of the primary beam

[3]Actually, the beam itself is largely unaffected, but particles interacting with the ROLU are prevented from triggering the data acquisition.

systems. Closest to the target is the micro-vertex tracker prototype, consisting of eight DSSSDs. This detector system, which is the main focus of this thesis, allows for position and energy loss measurements of outgoing charged particles. The target chamber and micro-vertex tracker are surrounded by the crystal ball (XB), a calorimeter consisting of 162 scintillating crystals covering a solid angle of almost 4π[4]. This detector is used for complete energy measurements of γ-photons and, in the forward direction, protons, scattered at large angles from the beam line.

Outgoing fragments at small angles relative to the beam line continue through the opening in the XB and reach the ALADiN dipole magnet. The trajectories of the fragments are deflected to different angles by the dipole magnet depending on their charge and momentum. Heavy charged fragments are bent into a trajectory passing through two scintillating fiber detectors (GFI) which provide horizontal and vertical positions, before reaching the ToF-wall (Time-of-Flight-wall). The ToF-wall is made of scintillating bars with readout at each end, making it capable of providing position and energy loss measurements in addition to the time measurement which is its primary purpose. Protons, which are bent to larger angles by ALADiN, instead reach the DTF, a detector similar to the ToF-wall. In front of the DTF are two drift chambers which provide positional measurements.

Neutrons, which are unaffected by the dipole magnet, will continue straight forward into the LAND-detector, which has given its name to the experimental setup. LAND consists of several layers of scintillating paddles arranged so that the paddles of each layer are perpendicular to the paddles of the adjacent layers. This, in combination with the paddles having readouts at both ends, provides a position sensitivity which allows for tracking of neutron interactions in the detector. Since the neutrons themselves cannot be detected by the scintillators, layers of iron placed between the scintillator bars act as a "converter", releasing charged particles, which can be detected, when neutrons collide with the iron nuclei[5].

2.3.2 FAIR and R^{3}B

GSI is currently being expanded into an international facility called FAIR, as shown in figure 2.3. A new, much larger, synchrotron will be built, allowing experiments with significantly higher energies [4].

As GSI is transformed into FAIR, the current LAND-setup will be transformed into the R^{3}B setup (Reactions with Relativistic Radioactive Beams) [5], eventually moving into a new cave behind the new synchrotron and Super-FRS. The function of the new setup will essentially be the same, but new detectors are required in order for the setup to be able to provide measurements at significantly higher particle energies with higher resolution and efficiency. As a part of this transformation, the crystal ball will be replaced by the CALIFA calorimeter, and inside it will be the new micro-

[4]The exception being a small opening for the beam line on the forward and rear sides of the detector.

[5]Conversion also occurs in the scintillators themselves, but with lower probability.

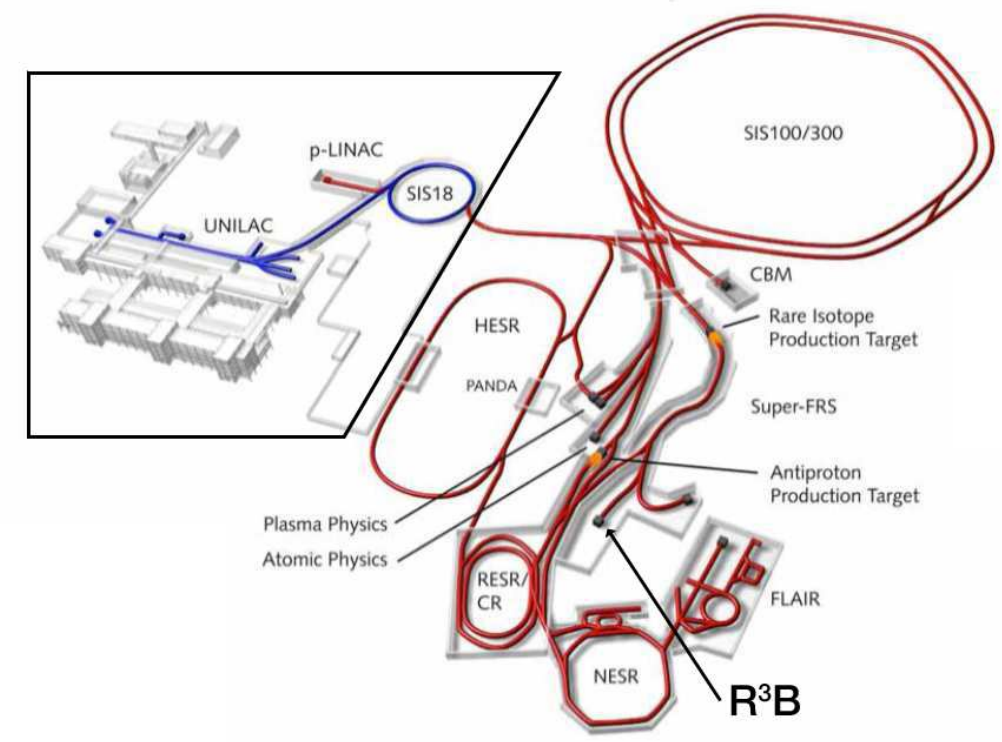

Figure 2.3: The planned FAIR facility. The framed section contains the existing facility, with current accelerators shown in blue. Original picture taken from [3]

vertex tracker. This new tracker will be functioning in the same way as the current tracker, but must be able to cope with the higher particle energies while providing higher accuracy and efficiency, as well as fit into the new calorimeter design. It can also be expected to have a larger total active area, leading to an increased number of readout channels. As such, most, if not all, of the issues with the current micro-vertex tracker will be of even greater concern in the new setup. Also, the new tracker will have two layers of sensors, making it capable of proper tracking of particles at all outgoing angles[6].

2.3.3 The S393 experiment

Most of the data analysed in this thesis comes from an experiment, S393, carried out at the LAND/R^{3}B-setup in the fall of 2010.

During the experiment, inverse kinematics reactions with relativistic light neutron-rich nuclei in the range $Z = 4$ to $Z = 10$, i.e., from Beryllium up to Neon, were studied. One focus of the experiment was to study cluster structures of ions near

[6]Please refer to section 4 for further details on the capabilities of the current setup

and beyond the neutron dripline through quasi-free knockout reactions[7] as a part of the quasi-free scattering program [6].

Quasi-free scattering refers to reactions where a simple projectile, such as a proton, scatters on a cluster[8] in a nucleus in such a way that the rest of the nucleus does not participate in the process. That is, the cluster can essentially be seen as a free particle.

[7] More specifically, (p, pn), $(p, 2p)$ and (p, α) reactions.

[8] Such as a single nucleon or larger structures such as deuterons, α-particles etc.

3. Silicon microstrip detectors

3.1 Semiconductors

Semiconductor properties of a material are directly related to its crystalline structure and can be explained by the electron band structure of such materials. In a single atom, the electrons occupy discrete orbitals, each with an associated energy. When several atoms are bound to form a molecule, their atomic orbitals split to form molecular orbitals. When the number of atoms becomes large, such as in a solid, this results in a huge number of orbitals with very small energy differences between them. The energy level structure can then be seen as continuous bands rather than discrete levels. These bands are separated by energy intervals where no orbitals are present, which are referred to as band gaps [7].

In conductors, the outermost band is partly filled with electrons regardless of temperature, which allows the electrons to move freely. In insulators and semiconductors, this band, called the valence band, is completely occupied. These concepts are illustrated in figure 3.1. Thus, electrons must be excited to the next band, the conduction band, in order to move freely. The distinction between semiconductors and insulators is the size of the gap between these two bands. If the band gap is of the order of 1 eV or less, the material is considered a semiconductor. Insulators typically have a 5 to 10 times larger band gap.

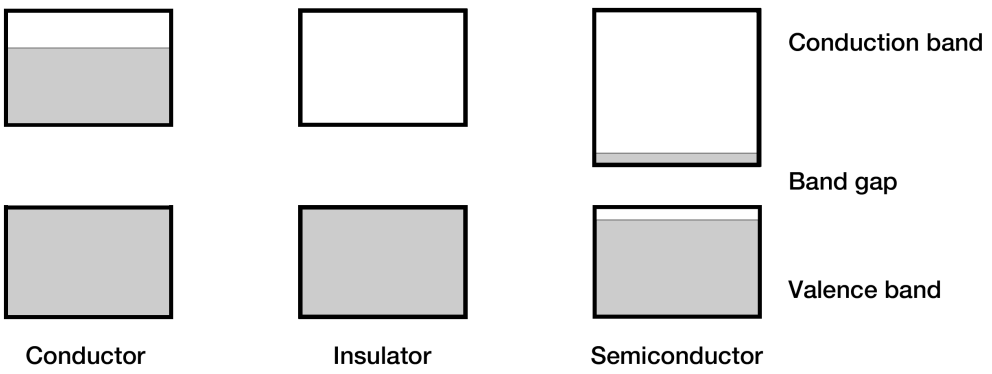

Figure 3.1: Illustration of the band structures of conductors, insulators and semiconductors. Grey indicates the filled electron energy levels.

3.1.1 Doping and *pn*-junctions

The characteristics of a semiconducting material can be modified by introducing impurities into the material's crystalline structure. This is process is called doping, and semiconductors containing such impurities are called extrinsic semiconductors. There are two kinds of doping, depending on the characteristics of the dopant:

p-doping introduces additional holes. Such dopants are referred to as acceptors.

n-doping introduces additional electrons in the crystalline structure. These dopants are known as donors.

The presence of dopants introduce new energy levels in the band gap, as shown in figure 3.2, which aid in the excitation of charge carriers. The gaps between the donor level and conduction band and between the valence band and the acceptor level are dependent on the dopant but typically have a magnitude of the order 10 meV.

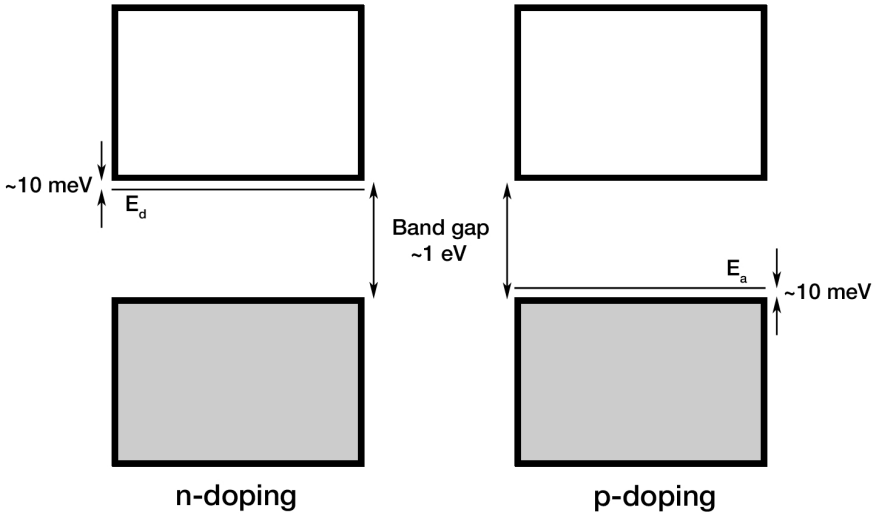

Figure 3.2: Illustration of the effects of doping. E_d and E_a indicate the energy levels introduced by dopants. The numbers should be interpreted as orders of magnitude rather than absolute values.

p- and *n*-type semiconductors can be combined to form a *pn*-junction. The electrons near the junction will then diffuse to the *p*-side, while holes diffuse to the *n*-side. This creates a region at the junction, known as the *depletion zone*[1], where there are no free charge carriers. The depth of this region is limited by the electric field across the junction, caused by the charge separation, which counteracts the diffusion process. A single *pn*-junction forms a *diode*.

[1] Also referred to as the *space charge region*.

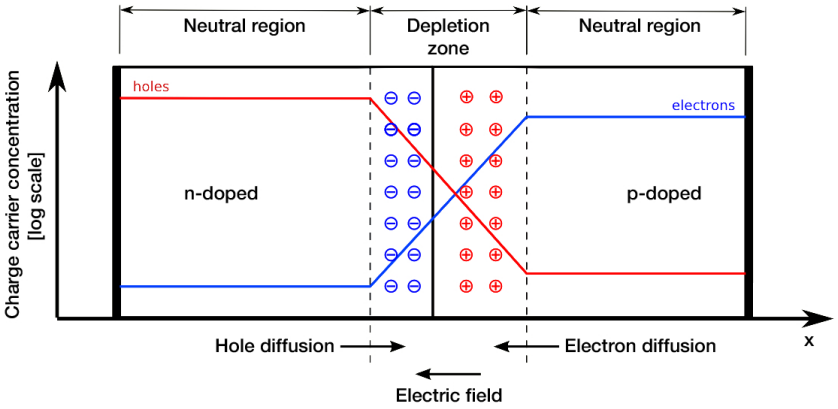

Figure 3.3: Illustration of a *pn*-junction showing the charge carrier concentrations and forces acting on the charge carriers.

3.2 Semiconductors as detectors

When a heavy charged particle enters the depletion zone of a *pn*-junction, it interacts with the material mainly by ionizing its atoms, depositing an amount energy in the material given by the so-called *Bethe-Bloch formula*[2] [1],

$$-\frac{dE}{dx} = \left(\frac{e^2}{4\pi\epsilon_0}\right)^2 \frac{4\pi z^2 N_0 Z\rho}{m_e c^2 \beta^2 A}\left[\ln\frac{2m_e c^2\beta^2}{I} - \ln\left(1-\beta^2\right) - \beta^2\right] \tag{3.1}$$

e**:** The electron charge.

ϵ_0**:** Vacuum permittivity.

z**:** Charge of incoming particle.

N_0**:** Avogadro's number.

Z**:** Atomic number of the stopping material.

ρ**:** Density of the stopping material.

m_e**:** The electron mass.

β**:** $\frac{v}{c}$ of the incoming particle, where v is the velocity and c the speed of light.

A**:** Atomic weight of the stopping material.

[2]This formula is not specific to semiconductor materials, but describes heavy charged particle interaction with matter in general. Two corrections, the *density effect* correction and the *shell* correction, are often added to the formula, but the qualitative behavior is largely the same.

I: The mean excitation energy of the atomic electrons in the stopping material.

For a specific material, this formula exhibits the proportionality

$$\frac{dE}{dx} \propto z^2 f(\beta) \tag{3.2}$$

where $f(\beta)$ is a function of only the particle velocity. Equation 3.2 clearly shows how energy loss measurements can be used to determine the charge of particles. For a given β, which can be determined by measuring the flight time of the particle between two detectors, the energy loss is directly proportional to the square of the particle's charge.

The energy deposited in a semiconductor diode by a passing heavy charged particle excites charge carriers from the valence band to the conduction band, with the amount of released charge carriers being proportional to the energy lost by the particle when passing through the material. The electrons and holes will then drift towards the n- and p-sides respectively, giving rise to a current which can be measured.

The depth of the depletion zone, d, is given by

$$d = \sqrt{\frac{2\epsilon (N_A + N_D)}{q_e N_A N_D} (V_{pn} - V_{ext})} \tag{3.3}$$

Where ϵ is the permittivity, N_A and N_D are the concentrations of acceptor and donor atoms, q_e is the electron charge, V_{pn} is the voltage over the junction caused by the charge carrier diffusion, and V_{ext} is an external voltage across the junction.

Clearly, by equation 3.3, the width of the depletion zone can be increased by applying an external reverse bias over the junction. As the active volume of the detector is equal to the volume of the depletion zone, semiconductor detectors are generally operated under a bias voltage large enough to deplete the entire detector volume.

The most commonly used materials for semiconductor detectors are silicon and germanium. Germanium has the advantage of allowing several centimeters of depleted volume, compared to only a few millimeters for silicon. The main disadvantage with germanium detectors is that they require very low operating temperatures which are generally achieved through liquid nitrogen cooling. The specific properties of these materials has led to silicon being used mainly for tracking detectors, while germanium is used in calorimetric applications [8].

3.2.1 Silicon microstrip detectors

Single-sided silicon strip detectors

A single-sided silicon strip detector (SSSSD), as seen in figure 3.4, consist of a bulk of n-doped silicon covered on one side by parallel strips of heavily p-doped silicon (heavy doping will henceforth be indicated by $^+$). Thus, it can essentially be seen as an array of p^+n-diodes. The surface in between the p^+-strips is covered by a thin layer of silicon oxide to reduce surface currents. The other side of the bulk is covered in a heavily n-doped silicon layer to assure good ohmic contact with the aluminium layer. The aluminium, which covers the strips as well as the entire backplane, serves as a contact for the readout of the sensor[9]. When a charged particle passes through the detector, it induces an electric signal in the nearest p^+-strips. The magnitude of this signal is proportional to the energy loss of the particle, while the position of the interaction along the axis perpendicular to the strips can be easily deduced from the location of the strips where the signal is induced.

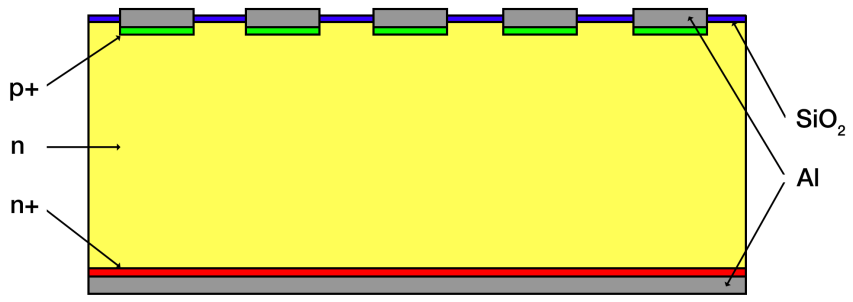

Figure 3.4: Cross-section of a single-sided silicon strip detector.

Double-sided silicon strip detectors

A trivial way of acquiring positional measurement in two-dimensions would be to simply use two perpendicular SSSSDs. This approach has a disadvantage in that it doubles the amount of material which the particle has to pass through, leading to an increased risk of particle scattering within the detector material[3]. A better solution is to instead use a double-sided silicon strip detector. Such a detector is essentially a SSSSD in which the backplane has been replaced by a layer of parallel n^+-doped strips orthogonal to the p^+-strips. As shown in figure 3.5 there are also p^+ doped strips implanted in between the n^+ strips. This is done to increase the interstrip resistance in order to prevent leakage currents.

[3]In addition to being a rather costly.

The p^+ side of a DSSSD is also referred to as the *junction side*, or more commonly, the S-side, while the n^+ side is referred to as the *ohmic*- or K-side. This thesis will henceforth use S and K to refer to the different sides of the DSSSD detectors. Due to the differences between the two sides in terms of main charge carriers and physical layout, they exhibit somewhat different properties.

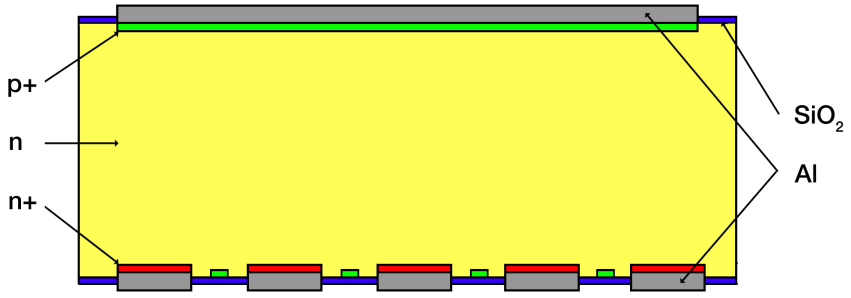

Figure 3.5: Cross-section of a DSSSD. Note that the top layer has the same structure as in figure 3.4, but the perspective is rotated by 90°.

As an ion passes through the DSSSD detector, the released electrons will be collected by the n^+ doped strips, while holes are collected by the p^+ doped strips. Each side will then independently provide an energy loss measurement, as well as a position measurement along the direction perpendicular to its strips. Combining the measurements from both strip planes allows for a two-dimensional position measurement.

Capacitive coupling

As hinted at in the previous section, a SSD has an intrinsic spatial resolution equal to the distance between its strips. Thus, one could make a detector with arbitrarily high resolution simply by increasing its strip density, the limit to the resolution depending only on how fine structures one can physically manufacture. However, if one wishes to have a large detector area, such an approach inevitably leads to a staggering amount of readout channels. A solution to this problem is to use capacitive coupling between the strips, and to only read some of them out, without losing resolution.

As a particle interacts near one of the floating strips, say strip n, the charge is divided into three parts, Q_b, Q_l and Q_r. Denoting the total capacitance between strip n and its nearest readout strips to the left and right by C_l and C_r respectively, and the capacitance between the strip and the backplane by C_b, there is a proportionality,

$$Q_b \propto C_b, \tag{3.4}$$

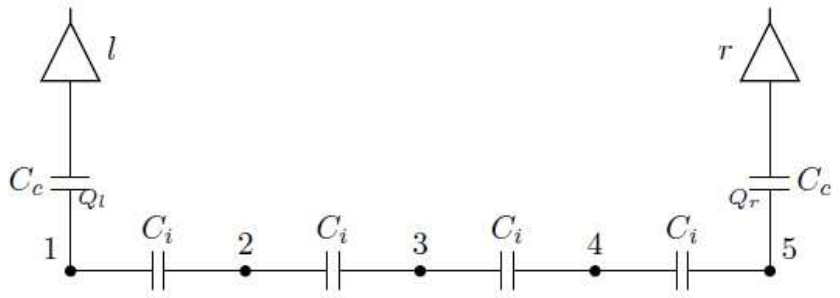

Figure 3.6: A schematic illustration of the concept of capacitive coupling. The numbers represent strips, with strip 1 and 5 being read out.

$$Q_l \propto C_l, \tag{3.5}$$

$$Q_r \propto C_r. \tag{3.6}$$

The charge Q_b remains on the strip, while Q_l and Q_r propagate to strips $n-1$ and $n+1$ respectively. The charge propagating to the neighbouring strips is once again divided into three parts with the same proportionality as before (although it should be noted that C_l and C_r now take different values). This process repeats until the charge is collected at the readout strips. The proportionality between the charge arriving at the readout strips to the left and right of the interaction point can now be used to determine the position of the interaction without having to read out every strip [10].

This method does however introduce some new issues. One is the fact that some charge will be lost on the floating strips, making the signal weaker. Another, which is of greater importance in the context of this thesis, is that the amplitudes of the readout signals will depend on the interstrip hit position, η, defined as the position of the hit, in units of strip counts, with regard to the nearest readout strips[4].

The capacitive coupling causes the charge from a passing particle to be distributed over several strips. Thus, determining the position and energy of an interacting particle is no longer as simple as determining which strip has been activated and the magnitude of its signal. Instead, the position of the interaction will now be determined by the peak of the charge distribution, and the energy by its (discrete) integral.

In reality, the capacitive coupling is more complex than what has been described here. A more accurate description would also consider coupling between the front-

[4]This is discussed in more detail in section 5.1.4.

and backplanes of the detector as well as between second neighbours. Despite the simplifications, this description still captures the basic functional properties of the detectors [11].

4. The micro-vertex tracker

4.1 Overview

The micro-vertex tracker at the LAND setup consists of eight DSSSD detectors which are located inside the target chamber. Four of the DSSSDs are placed to form an open box directly behind the target for detection of recoil protons. The remaining four are positioned in the beam line, two in front of the target and two behind the box as shown in figure 4.1. These detectors are used for charge identification and tracking of incoming and outgoing heavy charged particles[1].

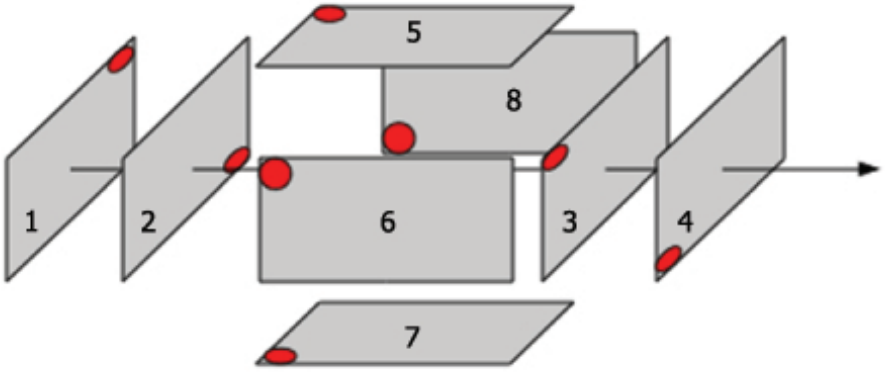

Figure 4.1: Orientation of the eight DSSSDs of the micro-vertex tracker. The red dots indicate the coordinate origins of each sensor and the numbers correspond to the names of the detectors in the *land02* unpacker ("SST1", "SST2", etc.).

All of the eight DSSSDs making up the micro-vertex tracker are built to the same specifications, originally developed for the experiment [12]. They each have an active area of $72 \times 40\,\text{mm}$ and a thickness of $300\,\mu\text{m}$. A DSSSD with attached front-end electronics is shown in figure 4.2, which also shows the alignment of the S- and K-side strips.

[1]The term "tracker" is used somewhat loosely here, as two full sensor layers would be needed in order to really make it a tracker. I.e., it currently only has tracking capabilities along the beam line.

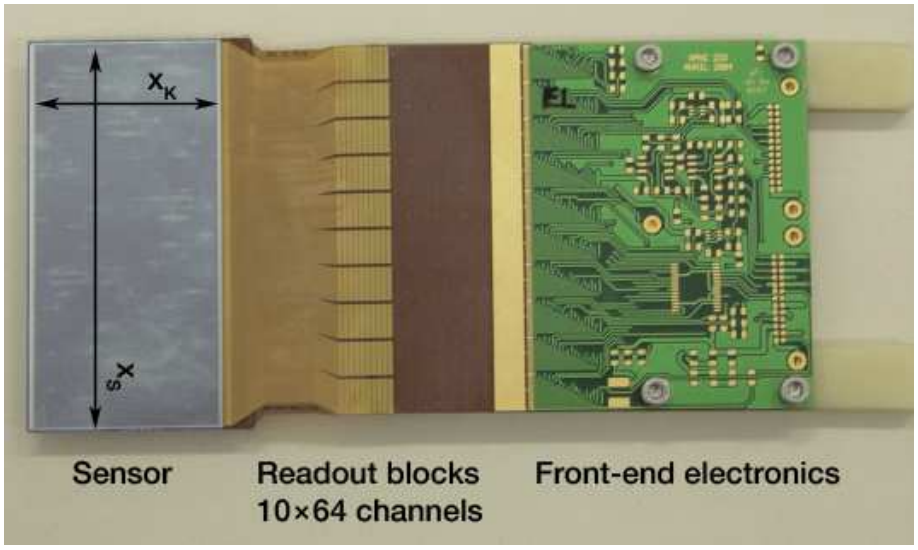

Figure 4.2: Photograph of a DSSSD. x_S and x_K indicate the axes along which the S- and K-sides measure the position. The orientation of the strips on respective sides are perpendicular to these axes. The readouts for the K-side are on the back of the detector module.

The S-side has strips implanted with an intermediary distance, referred to as the *implantation pitch* of 27.5 μm. Every fourth strip is connected to the readout, giving a *readout pitch* of 110 μm, with the remaining strips participating through capacitive coupling as discussed in section 3.2.1. The K-side has an implantation pitch of 104 μm with readout on all of its strips (i.e., the readout pitch is equal to the implantation pitch). With the given dimensions of the sensor, this adds up to 640 readout channels on the S-side and 384 channels on the K-side [13].

4.2 Front-end electronics and readout

The DSSSD strips are read out using VA_hdr9a chips manufactured by IDEAS Norway. These chips provide a large dynamic range and high density of input channels. Additionally, the input pitch of the chips is 96 μm which fits well with the sensor's readout pitch. Its low power consumption allows it to be mounted on the sensors inside the vacuum of the target chamber. Each VA-chip handles 64 strips, giving a total of ten chips for the S-side and six chips for the K-side signals.

Digitisation of the analog signals from the FEE is done using custom-designed NIM[2]-format modules called SIDEREMs. The SIDEREMs act as an interface between the FEE and the DAQ-system[3], accepting event triggers from the DAQ-system and re-

[2]Nuclear Instrument Module, a standardised format for electronic modules.
[3]Data AcQuisition-system. The electronics responsible for triggering measurements and collect-

turning digitised signal measurements [17]. Each SIDEREM is responsible for digitising the 1024 channels of a single detector. The signals from the FEE are fed serially to the ADCs of the SIDEREMs through three output lines, two output lines for the S-side chips and one for the K-side.

4.3 Unpacking

4.3.1 The *land02* unpacker

The LAND experiment uses a program suite called *land02* for event unpacking, calibration and reconstruction [14][15]. Data can be unpacked to different levels depending on which aspects one wishes to study. For the DSSSDs, the contents of these levels are:

RAW Data is represented in channel units (12 bit, 0-4095).

TCAL Contains pedestal-subtracted, common-noise-corrected and gain-adjusted energies. Strips are split into S-side (the first 640 strips) and K-side (the remaining 384 strips).

SYNC Same structure as TCAL, but with any non-significant energies removed. Strips with energies larger than 4 sigma are kept along with any neighbours above one sigma

DHIT Represented with cluster parameters. Individual strip information is lost.

HIT Combines the hits of the S-side and the K-side.

The *land02* unpacker is capable of unpacking the raw data to n-tuples compatible with *ROOT*, a software package developed at CERN [16]. *ROOT* essentially consists of a C++ interpreter along with a set of libraries designed for data analysis, visualisation and calculations within the field of particle physics.

4.3.2 Data formats

The original format used to store DSSSD data is shown as the "Old" format in figure 4.3. This has since been improved by implementing non-destructive preprocessing and Huffman coding, reducing the volume of data from 32 to roughly 3.5 bits per channel. However, the current format has the disadvantage of storing the signals from all read-out channels for each event. Due to the large amount of channels, this still adds up to about 450 bytes of data stored by each detector for each event. The

ing the measurement data.

large volumes of data require large amounts of disk space for storage, as well as making offline unpacking and analysis more time consuming. With the substantially greater number of channels expected in the future R^{3}B-setup, this issue may be of even greater concern.

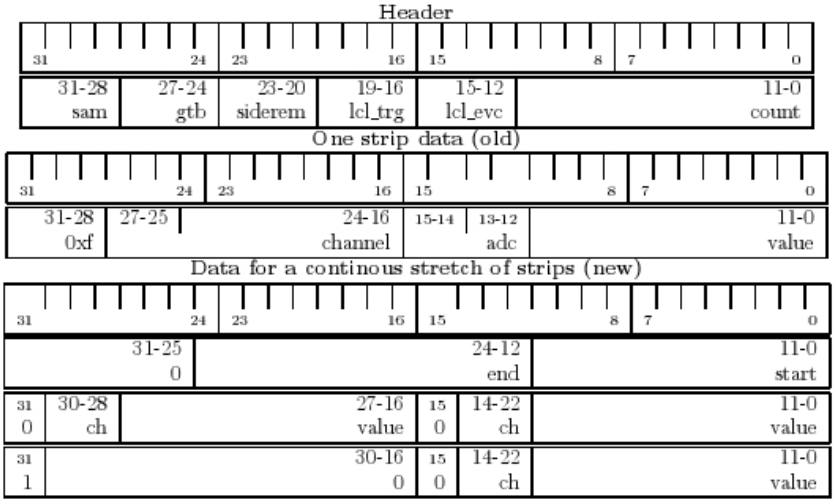

Figure 4.3: Comparison between the original ("Old") DSSSD data format and the data format output by the *siderem01* unpacker ("New"). Note that the current Huffman-coded format is not shown.

In order to reduce the amount of data, a method to filter out the empty channels, which is commonly referred to as zero-suppression, is highly desirable. A common approach to zero-suppression is to simply remove any channels below a threshold, which is determined during the experiment by regularly taking data from empty events where no ion has passed through the setup. This approach is, however, not quite satisfactory when applied to the DSSSDs as the baselines of the VA-chips tend to shift when large amounts of charge is collected [18]. Thus, thresholds calculated from empty events will be too high, leading to the "tails" of clusters being suppressed[4].

Alternative data format and the *siderem01* unpacker

The *siderem01* unpacker has been written specifically for testing an alternative, zero-suppressed data format for DSSSD data [19]. The aim is to eventually implement this data format into the SIDEREM modules connected to the DSSSDs of the micro-vertex tracker in order to reduce the amount of data produced by the detector system.

[4]This zero-suppression method was used by the old format, and is the reason why it was abandoned.

The reduction step of this alternative data format avoids the previously discussed zero-suppression problem by not looking at the absolute amplitudes of the signals, but rather at the pairwise difference between amplitudes of adjacent channels. Based on these principles, the data is provided as "stretches", with each stretch containing the individual strip signals of a single cluster, or possibly a set of overlapping clusters. Hence, most non-significant channels are filtered out, greatly reducing the amount of data from each event. In addition, the data is stored in a more effective way, and may be Huffman encoded to further reduce the required bandwidth and disk space.

The data format output by the *siderem01* unpacker, shown as the "New" format in 4.3, is significantly different from the original data format. Just like the original format, there is a 32-bit header for each detector and event. Following this is stretch-wise data, with each stretch consisting of a sub-header specifying the start and end of the stretch followed by the channel numbers and signal values for all of the strips included in the stretch. Since all the necessary overhead information is included in the sub-header, each 32-bit chunk can now hold the values from two strips rather than just one.

Currently, the *siderem01* unpacker is in an unfinished state. In order to able to use it within the thesis work, some debugging and modification of the code had to be done. Among other things, the unpacker has no file output implemented in its current state. This was worked around by implementing a very crude text-file output. The text files could then be imported into MATLAB for further analysis.

5. Analysis and calibration

As the unpacked experiment data, regardless of which unpacker is used, is presented in the arbitrary unit of ADC counts and strip indices, several steps are required in order to extract physical quantities. The following section will describe how this is currently achieved, discussing some of the problems faced by the current method. An alternative approach for event reconstruction is also introduced, which is further studied and evaluated in this thesis.

5.1 Basic concepts

Before describing any method for DSSSD data analysis, some basic properties of the signals output by the detector system should first be discussed.

5.1.1 Signal components

In the following sections, strips are referred to by indices $i, j, ...$ and their signals as $s^e_{i,j,...}$ for the event e.

Ideally, in an empty event, that is, when no ion is passing the detector, the signals of all of the DSSSD strips should be zero,

$$s^e_i = 0. \tag{5.1}$$

However, due to imperfections in the electronics, this is in reality not the case. Firstly, each individual strip has some offset, known as its *pedestal*, which is constant for that strip,

$$p^e_i = p_i. \tag{5.2}$$

Secondly, slowly drifting parameters in the setup, such as instabilities in the power supply, introduce an additional common offset for all strips, a *common baseline* for each event,

$$b^e_i = b^e. \tag{5.3}$$

Finally, there is some resolution-dependent error, ϵ, for each strip and event. Thus, in an empty event, one can expect a signal for each strip given by

$$s_i^e = p_i + b^e + \epsilon_i^e. \tag{5.4}$$

When an ion passes the detector, an additional component, q, is introduced from the collected charge carriers,

$$s_i^e = p_i + b^e + \epsilon_i^e + q_i^e. \tag{5.5}$$

Clearly, only q is of any interest when one wishes to extract physical quantities from the measured signals. Therefore, the magnitude of p and b must somehow be determined. This can be accomplished by simply taking regular measurements of empty events. The measured signals from empty events can then be used as estimates for the pedestals of each channel and, by comparing successive measurements, baseline shifts can be detected[1].

5.1.2 Energy loss

For each hit in the DSSSD detectors, a signal is seen in a number of adjacent strips, $N_{S,K}$, on the S- and K- sides respectively. Each such set of firing strips is referred to as a cluster. The energy loss of a particle is proportional to the sum of the charge measured in the participating strips on each side, i.e.,

$$\Delta E \propto S_S = \sum_{i=i_{start}}^{i_{end}} s_i \propto S_K = \sum_{j=j_{start}}^{j_{end}} s_j. \tag{5.6}$$

Where i_{start}, j_{start} and i_{end}, j_{end} indicate the indices of the first and last strips of the cluster, i.e., $i_{end}, j_{end} - i_{start}, j_{start} + 1 = N_{S,K}$. Note that the energy loss can be determined from the corresponding S- and K-side clusters independently. Assuming that both sides are properly calibrated, the proportionalities in equation 5.6 above become equalities. It should be noted that the different sides have different characteristics, meaning that one side may give a more accurate result than the other for a given energy. Generally, the K-side exhibits better resolution for lower energies, but is more easily saturated than the S-side.

5.1.3 Hit position

The hit position can be determined by calculating the center of gravity of the cluster.

[1] There are however some problems with this approach, as discussed in 4.3.2.

$$x = \frac{1}{S_S} \sum_{i=i_{start}}^{i_{end}} s_i \cdot i, \tag{5.7}$$

$$y = \frac{1}{S_K} \sum_{j=j_{start}}^{j_{end}} s_j \cdot j. \tag{5.8}$$

This gives the hit position in units of strips. Thus, to get the hit position in SI units, this result has to be multiplied with the strip pitch. Note that, to get both the x- and y-position of the hit, we must use the signals on both the S- and K-sides of the detector.

5.1.4 Corrections

There are some corrections that need to be made in order for the previously described calculations to give accurate results. First, we need to define the interstrip hit position, η, as given by

$$\eta_S = \{x\} = x - \lfloor x \rfloor, \tag{5.9}$$

$$\eta_K = \{y\} = y - \lfloor y \rfloor. \tag{5.10}$$

Obviously, this means that η will be in the unit range,

$$\eta_{S,K} \in [0, 1[. \tag{5.11}$$

Thus, a value of $\eta = 0$ indicates a hit right on a readout strip, whereas $\eta = 0.5$ indicates a hit right between two readout strips and $\eta = 1$ would mean a hit right on the next strip.

By plotting the cluster sums against η, an example of this is shown in figures 5.1 and 5.2, it can clearly be seen that the proportionality between the cluster sum and the energy loss is not constant, but rather varies significantly with η.

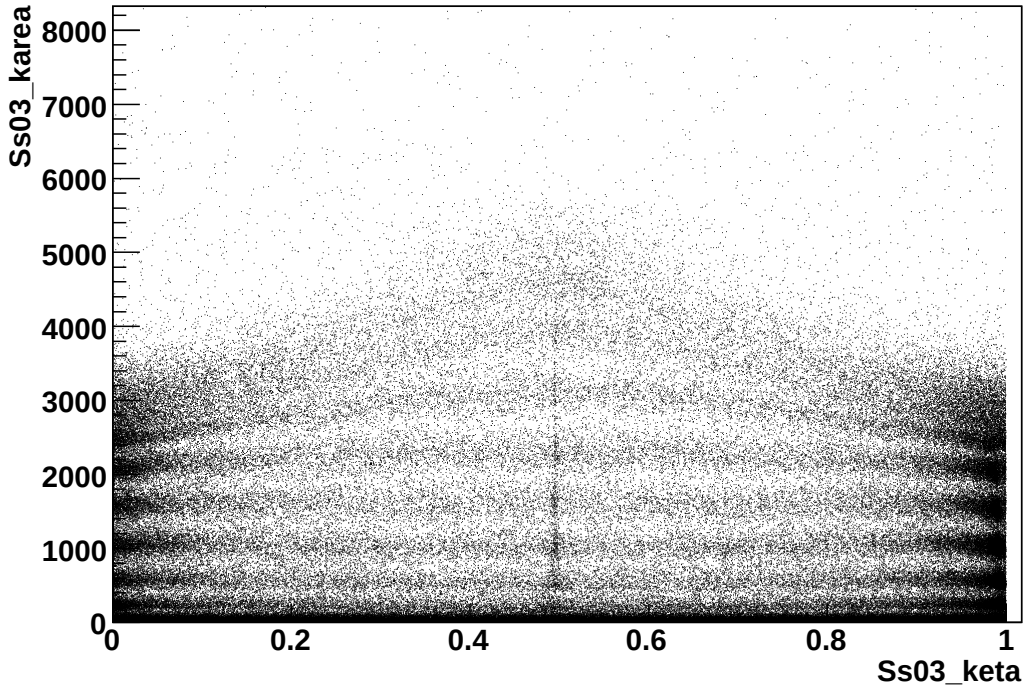

Figure 5.1: η dependency of the cluster sum in the K-side of SST3.

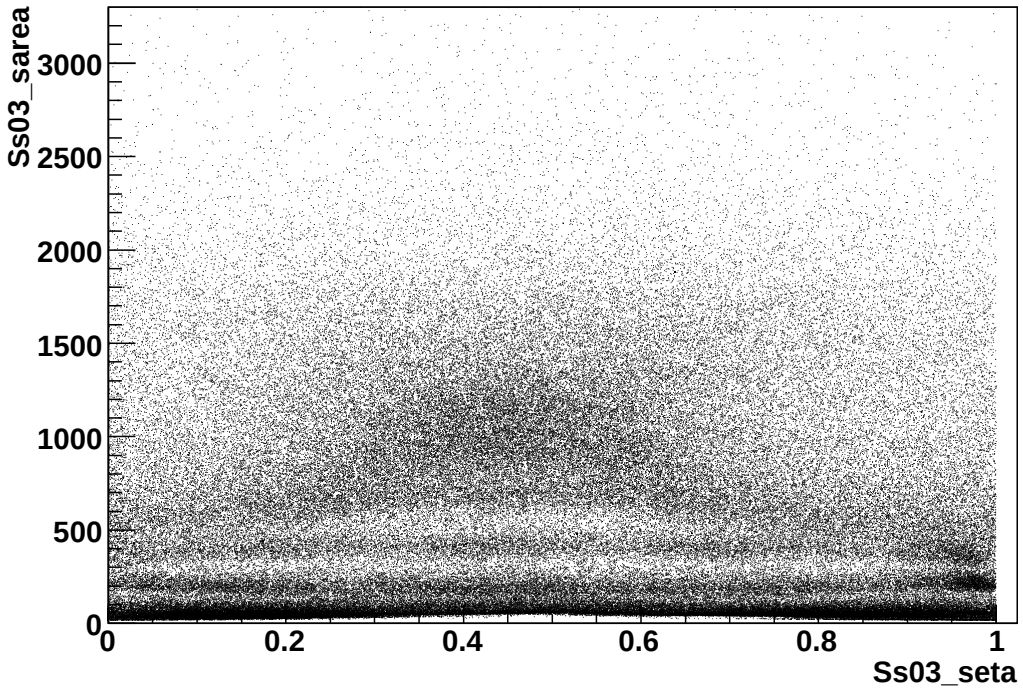

Figure 5.2: η dependency of the cluster sum in the S-side of SST3.

Thus, there appears to be a proportionality

$$S \propto g(\eta). \tag{5.12}$$

Where g is some function which varies with η. Furthermore, the η dependence appears to vary with the total cluster charge, i.e.,

$$g = g(S, \eta). \tag{5.13}$$

In reality, this means that η-dependency corrections must be performed individually for each ion charge[2].

Furthermore, each channel has an individual gain, μ, which is a property of the FEE. This means that the quantity s is not what will actually be read out. Rather, the signal that is read out from each strip, ξ will be

$$\xi_i = \mu_i s_i. \tag{5.14}$$

[2]However, all charges do not necessarily exhibit any η-dependency.

To complicate things even further, it has been claimed [20] that the magnitude of the gain is not constant, but dependent on the magnitude of the strip signal. This dependency is illustrated in figure 5.3.

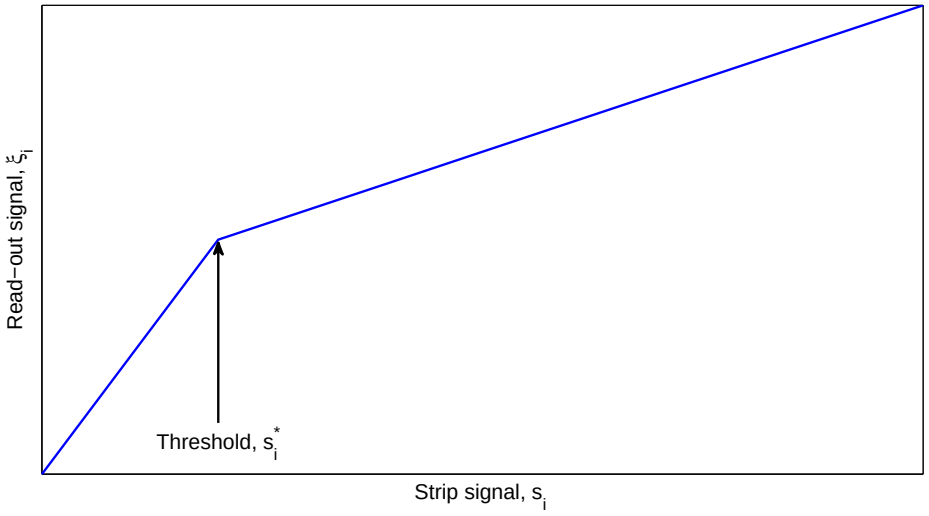

Figure 5.3: An illustration of the gain behaviour of the FEE. The plot shows the read-out signal from the FEE for a given strip as a function of the strip signal before the FEE. There are two regions with different gain factors, making the read-out signal from the FEE behave as a piecewise linear function of the signal from the DSSSD strip.

This means that

$$\mu_i = \mu_i(s_i). \tag{5.15}$$

The total read-out signal is then given by

$$S = g(S, \eta) \sum_{i_{start}}^{i_{end}} \mu_i(s_i) s_i. \tag{5.16}$$

In order to reach the full potential of the DSSSD detectors, all of these (and perhaps more) corrections must be correctly applied before the energy loss and position is calculated.

5.1.5 Dead strips

Another issue which may lead to a reduced accuracy is that of dead strips. These are strips which, for some reason, are not properly read out. This may be due to e.g. a broken bonding wire. Such strips are easily identified by simply counting the number of events above some threshold for each strip [21], as illustrated by figure 5.4.

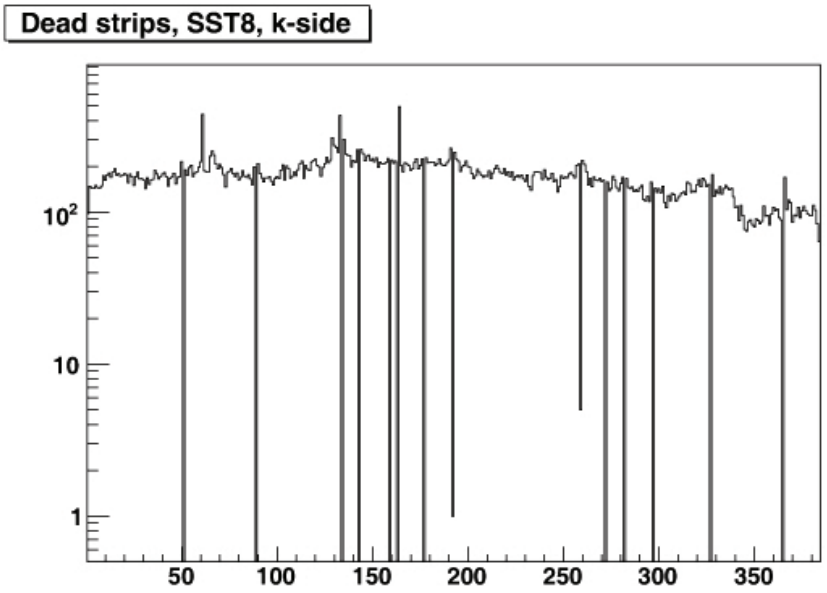

Figure 5.4: Signal counts with amplitudes greater than 20 ADC counts for each K-side strip of SST8. Dead strips can be identified by the lack of counts. Also notable is the tendency of strips near dead strips to have slightly higher counts than the other strips.

Unfortunately, handling the dead strips during the data analysis is not quite as straightforward as finding them. Assuming that dead strips are essentially short-circuited, so that any charge collected by such strips is lost, a simple approach to recovering clusters containing dead strips would be to assign some expected value to the strip. In the case of a wide cluster, one could argue that taking the average of the two neighboring strips would give a reasonable approximation to the lost charge. This approach is less valid if the cluster forms a sharp peak, and invalid if that peak coincides with the dead strip. This is a greater concern on the K-sides of the DSSSDs, as they usually have more narrow clusters.

Also, it is not clear that one can assume the charge collected by a dead strip to be lost. Rather, it may be fully or partially collected by its neighboring strips. One must then not only account for the dead strip itself, but also for its effect on neighboring strips. A closer look at the data in 5.4 seems to indicate that the presence of dead strips affect the signals of nearby strips as well.

There is also the option to try to recover the missing energy from the other side of the detector. Assuming that the S- and K-sides are properly calibrated, the cluster sum of a specific hit should be the same on both sides. However, missing strips may lead to mismatching of the S- and K-side clusters in the case of several hits. Also, for large deposited energies, the K-side may have saturated, making it essentially useless for energy measurement.

Furthermore, a cluster may contain not only one but several dead strips, making reconstruction even more difficult.

5.2 Cluster fitting

An alternative approach to reconstruction of DSSSD events is to attempt a function fitting of the clusters. If such a method can be successfully implemented it would have two great advantages. Firstly, it may be able to accurately reconstruct clusters containing missing or distorted energies due to dead strips. Secondly, it may be able to recover proton hits which have been "lost" in the signal tails from heavier fragments, as illustrated by figure 5.5. Such an approach would primarily be of interest for the S-sides, as K-side clusters are generally very narrow, often consisting of only one or two large signals with small "tails".

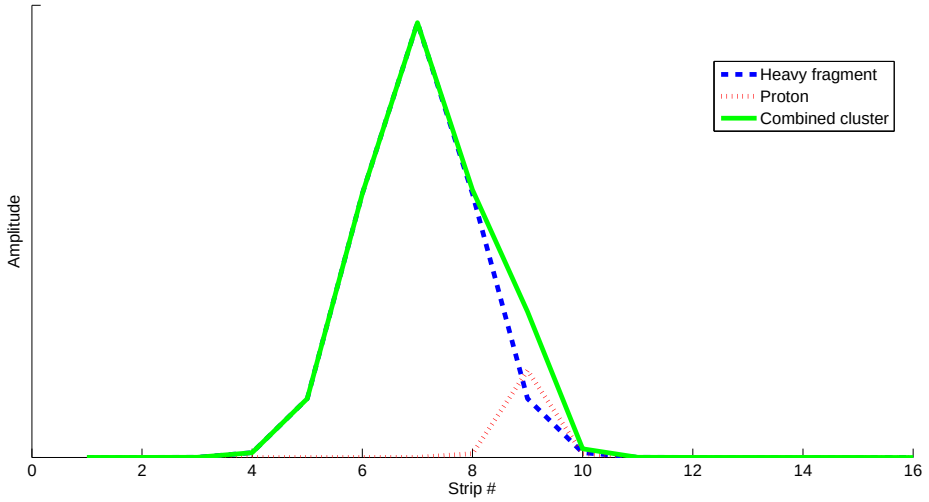

Figure 5.5: An example of overlapping clusters. The small proton cluster is obscured by the heavier fragment. Reconstructing this event using the basic method described in 5.1 would lead to the proton being "lost" while the position and energy loss measurements for the heavy fragment would be incorrect.

Assuming that the cluster shapes can be described by some function (or, in the case

of multiple hits, a linear combination of such functions) which varies slowly with the deposited energy and position (or, rather, η), one could recover these quantities by fitting such functions to the cluster shape. There has already been some work done to evaluate such a method [21]. Unfortunately, these attempts were largely unsuccessful as it turned out to be difficult to get good fits. The main problem with the approach is that clusters, even on the S-side, typically only have a handful of significant points, thereby making it difficult to fit a function with several degrees of freedom, such as a Gaussian, to the clusters.

5.2.1 Template clusters

A possible way to get around the more generalised fitting problem could be to instead have a set of "template cluster functions" for different energy and η intervals. Linear combinations of such template clusters could then be used to try and fit measured clusters. An attempt at finding such template clusters for the S-side of the detectors has been done using data from the S393 experiment. SST3 was chosen as the most suitable detector for this, as it sits in the beamline and thus sees a lot of hits over a large energy range. Furthermore, the S-side of SST3 has no dead strips to take into account, making the analysis a bit more straightforward.

After some debugging and slight modification of the *siderem01* unpacker, it was capable of providing stretches with cluster data in raw form, with adjustments done for the pedestals and baseline. For the calculation of template clusters, the stretches should ideally contain a single cluster from a single particle hit. Stretches containing either overlapping hits or multiple, separated, hits are undesirable and should be discarded. Many of the stretches output from the unpacker were unsuitable for the intended purpose, for varying reasons:

Noisy stretches were primarily a concern for low cluster sums. These contain many small clusters rather than a single, large, cluster. The high number of clusters in these stretches makes it improbable that they originate from actual ion hits.

Multiple cluster stretches are stretches containing multiple (usually only two) separated clusters that are close enough to be included in the same stretch. The clusters themselves are perfectly fine, but must be treated individually.

Wide cluster stretches are stretches containing abnormally wide clusters, possibly from overlapping hits. In the lower energy range, this may also be due to incorrect baseline determination.

Negative signal clusters contain one or more negative strip signals. The cause for this is unclear, it is most likely related to the unpacking process. This issue has also been described in [11].

In order to find cluster shapes representative of each interval the bad data stretches had to first be identified and removed. The remaining good stretches then had to be normalised and centered so that the peak positions coincide. The cluster sum was used as a normalisation factor for the strip signals of each cluster. Two methods for centering the clusters were implemented, centering based on the largest amplitude strip, and centering based on the two largest amplitude strips. The template clusters were then calculated as the mean of a large set of normalised and centered stretches, along with corresponding standard deviations.

Finally, an evaluation of the possibility to use the calculated template clusters was performed. This was done by attempting to match the normalised and centered clusters used for the calculations of the templates to the templates themselves and comparing the acquired results to the known characteristics of the clusters. As such, this test should be very easily passed if the method is to be useful for reconstructing more complicated clusters.

6. Results

6.1 Template clusters

6.1.1 Basic behaviour

DSSSD clusters with cluster sums between 200 and 1600 ADC counts were studied. The lower bound on the cluster sum range was set at 200 ADC counts in order to avoid the large amount of "bad" clusters found when accepting smaller clusters, while the upper bound was due to poor statistics in the data set for larger clusters. The clusters were sorted into sub-ranges with a width of 200 ADC counts, henceforth referred to as *cluster sum ranges*, which was found to be wide enough to give reasonable statistics for each sub-range.

The detector exhibits a symmetry with regards to η, as shown in figure 6.1. The behavior of clusters in the range $\eta > 0.5$ is the same as for clusters with $\eta < 0.5$, only mirrored. Based on this, the following results will mainly be presented only for $\eta \in [0, 0.5]$. Clusters were sorted into η-ranges with a width of 0.1. Thus, in the following discussion, η-values will be given with a one decimal precision so that $\eta = 0$ refers to the range $\eta \in (0.95, 0.05]$, $\eta = 0.1$ refers to $\eta \in (0.05, 0.15]$ and so on.

It was found that the cluster sum, in the ranges studied, acted essentially as a simple scaling factor on the cluster. That is, the shape of the cluster is solely dependent on η, as illustrated by figures 6.2 and 6.2. This means that the problem of finding normalised template clusters for a given value of η and the cluster sum in this range is reduced to finding templates only for different η-values.

There are however some slight differences between the different cluster sum ranges. Firstly, for the lowest range, the standard deviations of the sets of clusters are considerably larger than for the other ranges. This is due to the fact that it becomes more difficult to separate the "good" and "bad" clusters. Secondly, when going to the higher cluster sum ranges, the ratio of the maximum amplitude to the cluster sum starts to decrease slightly, possibly due to the nonlinear gain mentioned in section 5.1.4.

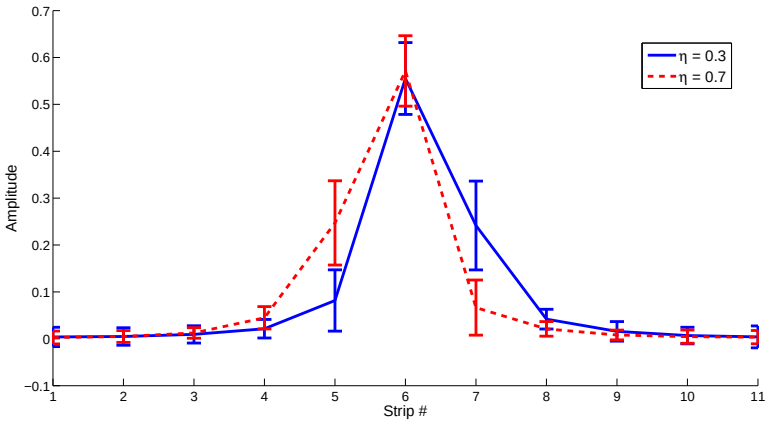

Figure 6.1: Example of the η-symmetry of cluster shapes. A cluster with $\eta = 0.7$ has the same shape, but mirrored, as a cluster with $\eta = 0.3$. The same goes for $\eta = 0.6$ and $\eta = 0.4$ and so on.

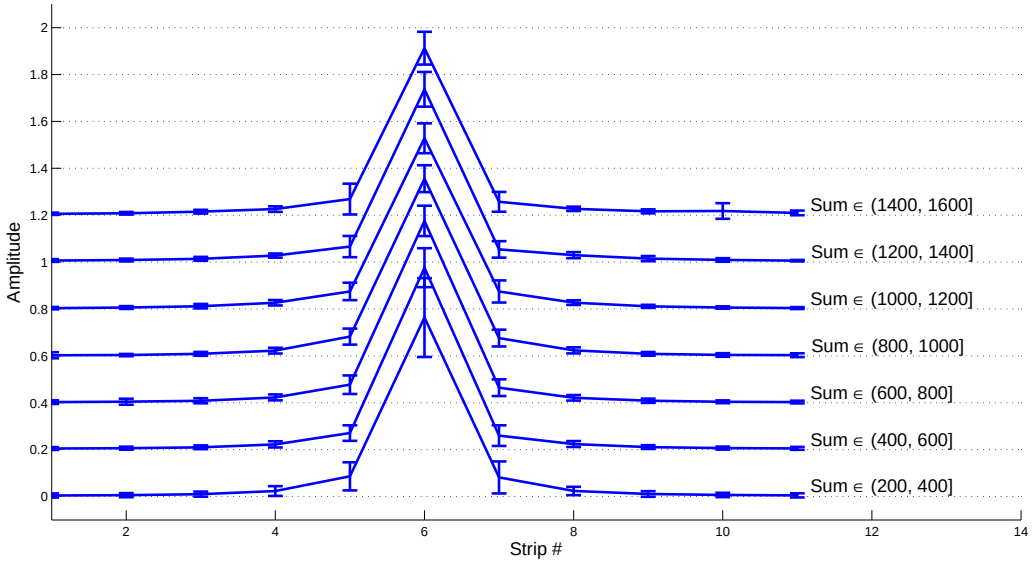

Figure 6.2: Normalised mean clusters calculated for $\eta = 0$ for different cluster sum ranges. The clusters have been offset on the y-axis in increments of 0.2 for clarity. The shape of the clusters is largely the same independent on the range, indicating that the cluster sum acts as a simple scaling factor.

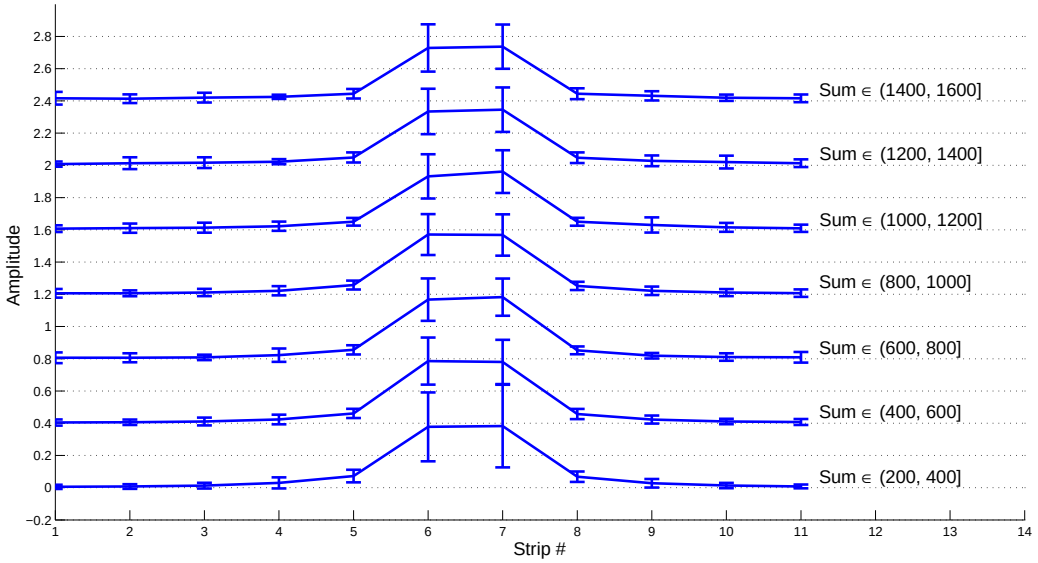

Figure 6.3: Normalised mean clusters calculated for $\eta = 0.5$ for different cluster sum ranges. The clusters have been offset on the y-axis in increments of 0.4 for clarity. The shape of the clusters is largely the same independent on the range, indicating that the cluster sum acts as a simple scaling factor.

6.1.2 Identification of bad stretches

Bad stretches were identified by comparing the largest amplitude of each stretch with the cluster sum calculated for the entire stretch. Figure 6.4 shows histograms of the ratio of the maximum amplitude to the stretch sums for two different η-ranges. An example comparison between a good and bad stretch is shown in figure 6.5.

As seen in figure 6.4, there is a relatively large amount of counts for a ratio of $0.1 - 0.2$ independently of the η interval studied[1]. These events were found to be unsuitable for the calculations. The second large "bump", varying in position with η contains mainly good stretches. These were selected for further analysis and sorted into different η and cluster sum ranges.

6.1.3 Centering

A comparison between the two methods of centering clusters before calculating their means is shown in figure 6.6. The total error was defined as the sum of the standard deviations for each strip in the cluster set for a given $\eta - range$, i.e., the summed

[1] Although not shown here, this is the case for all η-intervals

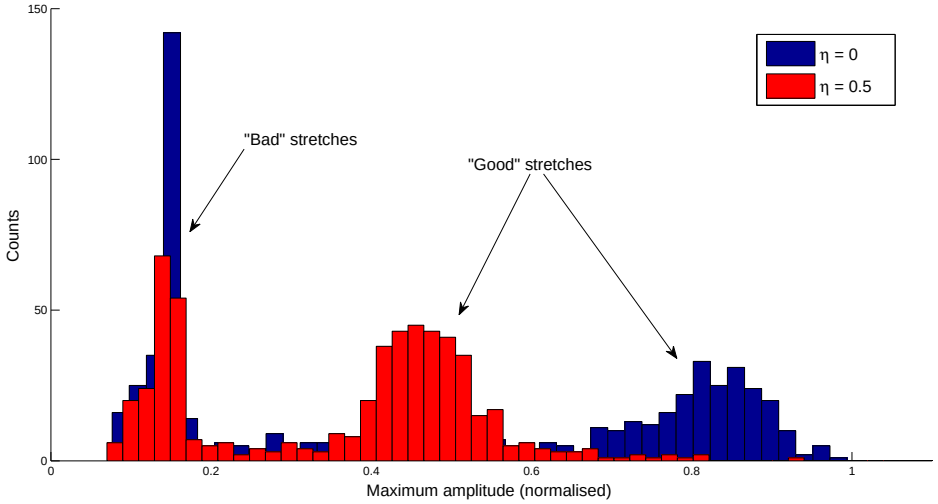

Figure 6.4: Distributions of the ratio of maximum amplitudes of clusters to their sums. This allows for the identification of "bad" clusters that are unsuitable for further analysis.

magnitudes of the error bars for the calculated template clusters. As expected, centering based on only the largest amplitude strip provides better results for hits near a strip, while centering based on the two largest amplitudes were better suited for η-values close to 0.5. Based on this, the results presented in this section were acquired using single-strip centering for $\eta \in [0, 0.3]$ and two-strip centering for $\eta \in [0.4, 0.5]$.

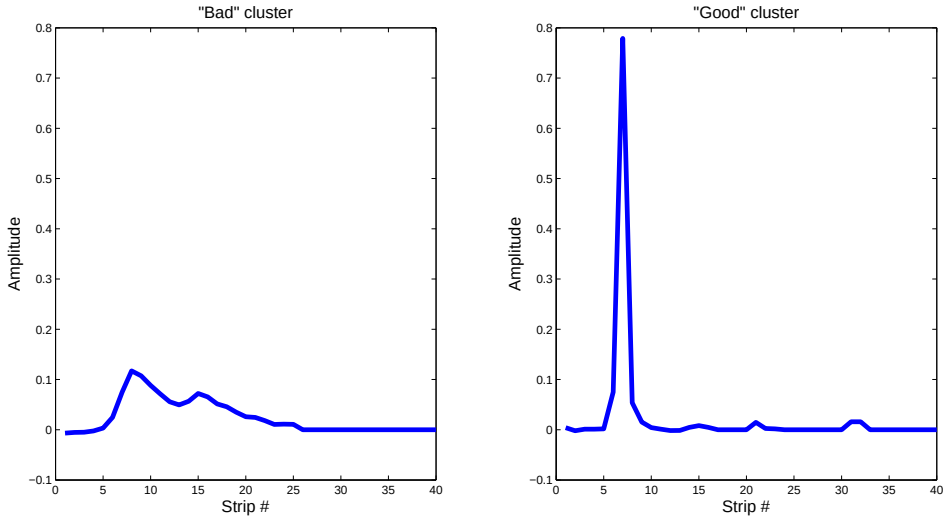

Figure 6.5: Example of bad (left) and good stretches. Both stretches are from the same cluster sum range and are normalised by their cluster sums.

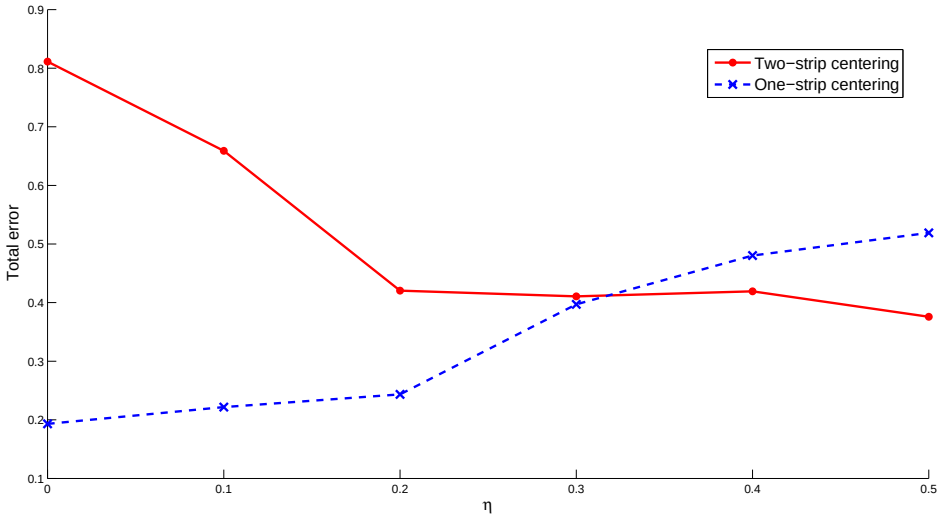

Figure 6.6: Total errors for calculated template clusters using single-strip or two-strip centering. The total errors are defined as the sum of standard deviations for all strips of a cluster set with a given η.

6.1.4 Calculated template clusters

Figure 6.7 shows the acquired template cluster shapes for different values of η. These were calculated from clusters with a cluster sum in the range $400-600$ ADC counts, as this range offered good statistics in the data that was used. However, as mentioned above, the shapes were found to be essentially identical in the adjacent cluster sum ranges. The clusters for each η-range were normalised by their cluster sums and centered as described in section 5.2.1. The template clusters were then calculated as the mean for each such set of clusters.

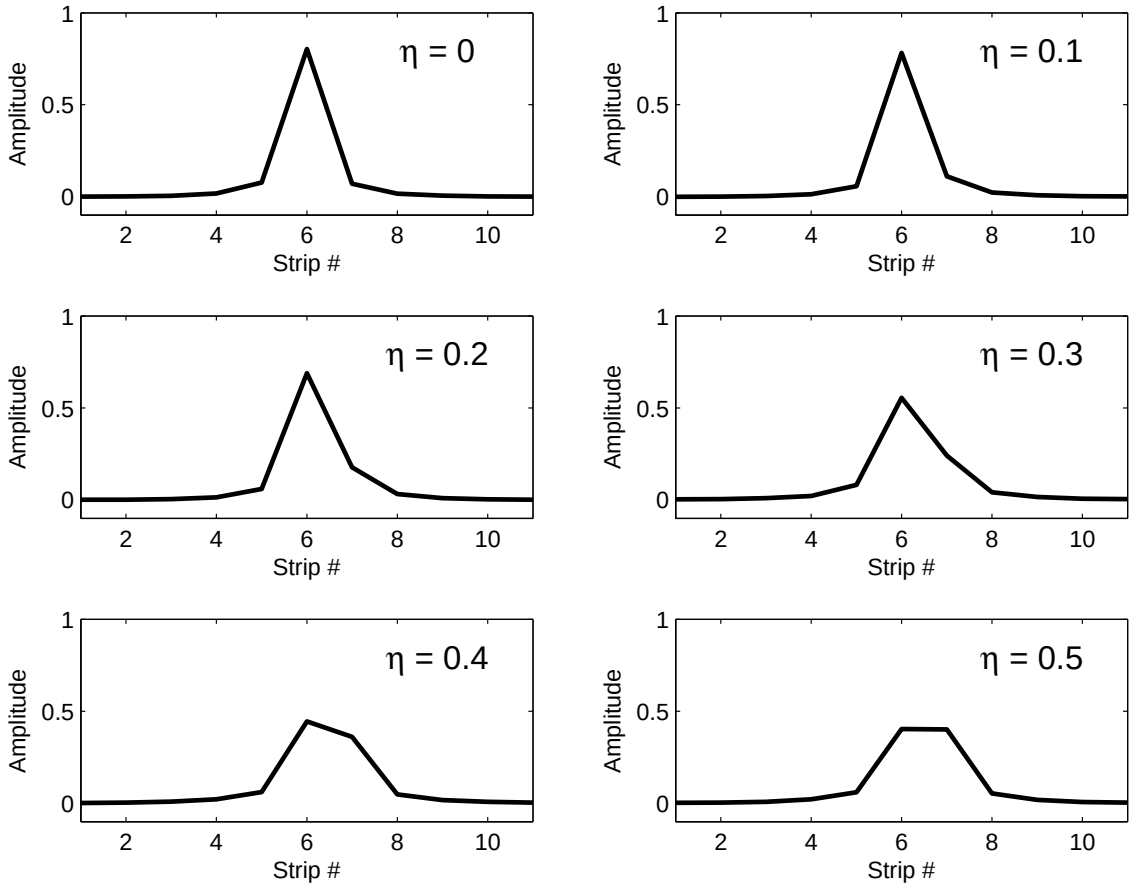

Figure 6.7: Template clusters calculated by averaging a large set of normalised and centered "good" clusters with sums ranging from 400 to 600 ADC counts.

There is an observable difference in the shapes of clusters with different η-values, and the behavior of the cluster shapes is quite predictable as η varies. Unfortunately, the differences between adjacent η-ranges is rather small compared to the magnitude of the standard deviations for the sets of clusters used to calculate the templates. As illustrated in figures 6.8 and 6.9, there is a large overlap of the error bars for adjacent η-ranges.

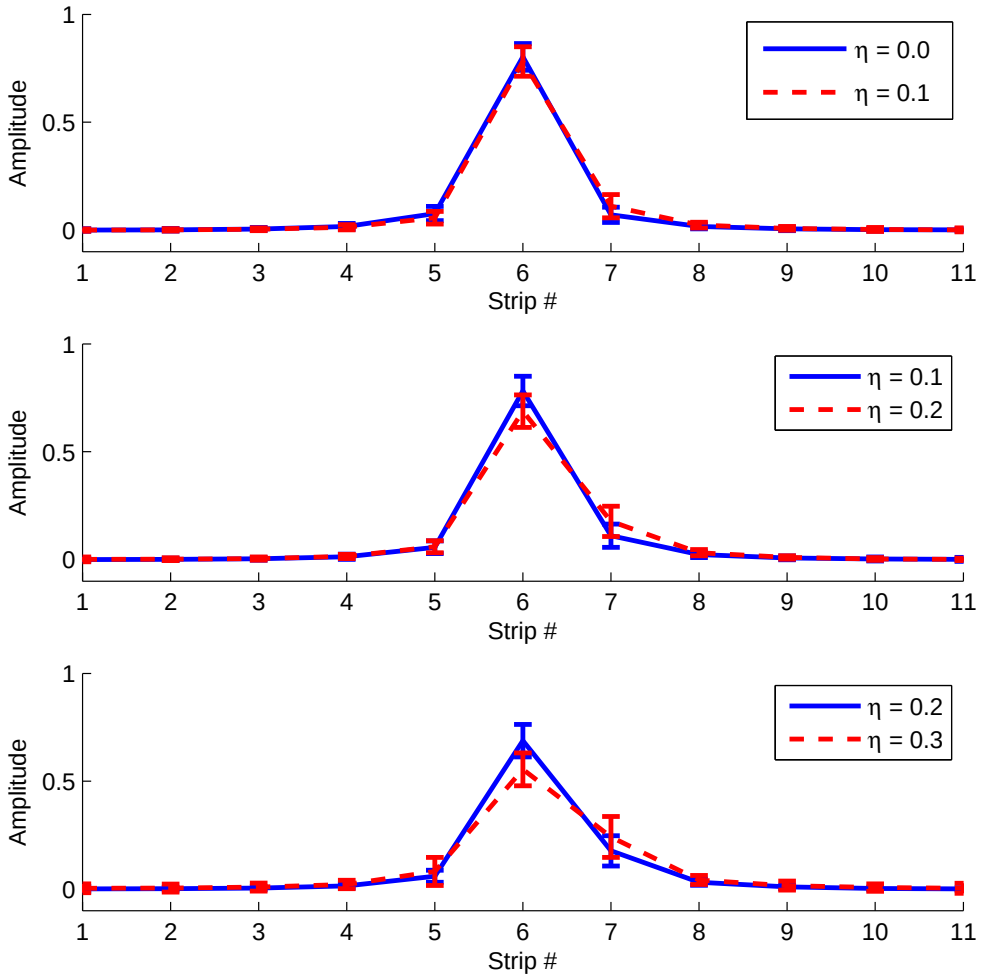

Figure 6.8: Comparisons between template clusters for adjacent η-values. The error bars indicate the standard deviation of the set of clusters used for the calculation.

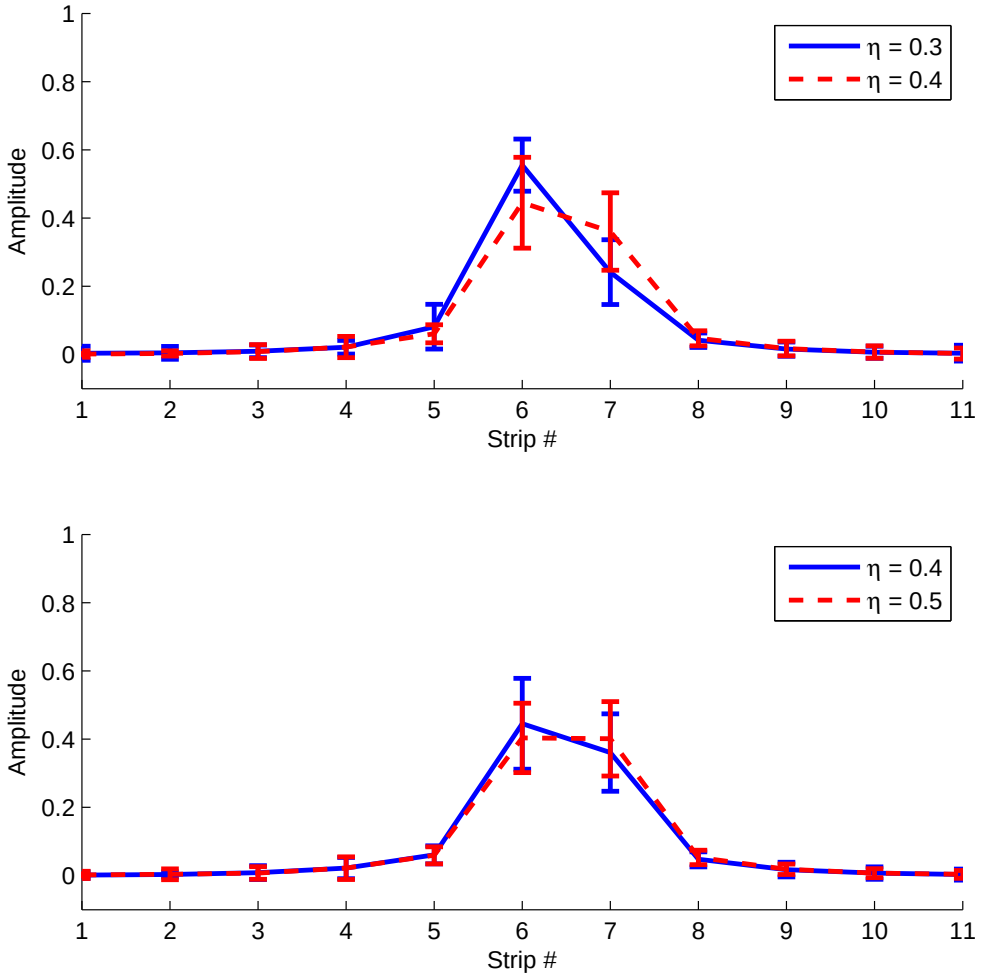

Figure 6.9: Comparisons between template clusters for adjacent η-values. The error bars indicate the standard deviation of the set of clusters used for the calculation.

6.1.5 η-reconstruction

Finally, the result of the "reconstruction test", as described in section 5.2.1, is presented in figure 6.10. Two different acceptance criteria were used, acceptance for only the correct η-range, and acceptance for the adjacent ranges as well. I.e., the maximum allowed errors in η are 0.05 and 0.15 for the two different criteria respectively. For the first acceptance criterion, although the success rate is relatively high for some η-values, the overall performance, an average success rate of roughly 50%, is far from satisfactory. This was expected based on the previously presented results. The success rate for the second criterium is however quite high with an average success rate of about 83%, meaning that most of the incorrectly determined η-values were assigned a value in an adjacent range.

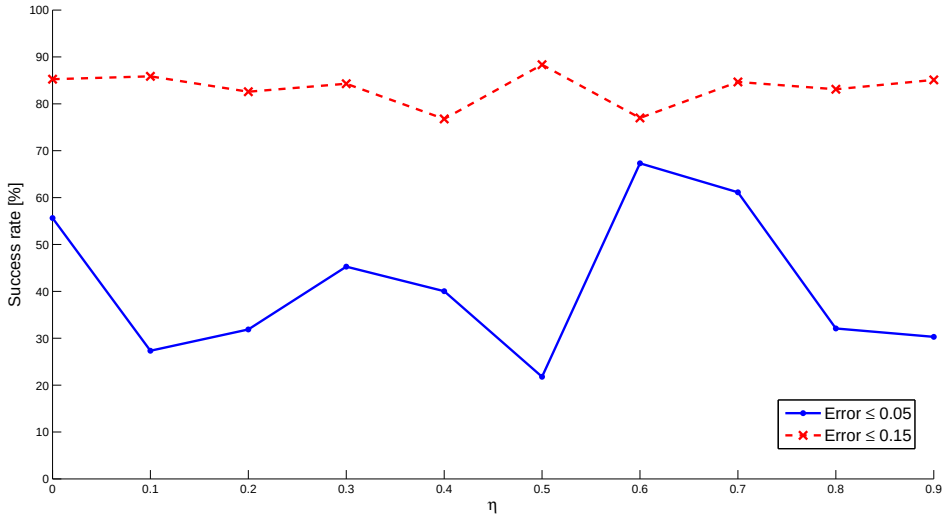

Figure 6.10: Success rate for the η-reconstruction test. The ratios of correctly determined η-values by matching clusters to the calculated template clusters are shown as a function of η. The results from two different acceptance criteria are shown, acceptance for only the correct η-range and acceptance for the adjacent ranges as well.

7. Conclusion and outlook

The micro-vertex tracker currently suffers from several issues related to the handling and analysis of measurement data. Lack of working online zero-suppression leads to the detector subsystem producing excessive amounts of data. As the LAND-setup is transformed into R^3B, an even greater number of channels is expected for the new micro-vertex tracker, making this issue even more pressing.

The event-finding method used by the *siderem01* unpacker, along with its more effective format for data storage, seems like a plausible solution to this problem, although there is a some work to be done before it is in a state where it may be considered as an alternative to the current unpacking code. In its current state, with some minor modifications, it may still be used as a tool for studying the behavior of the DSSSD modules as shown in this thesis.

The attempt at DSSSD event reconstruction using template clusters was largely unsuccessful. Although a clear difference in cluster shapes for different η intervals was observed, the standard deviations of the cluster sets used to calculate the templates were found to be too large for successful classification of clusters based on the templates. When testing the method by attempting to reconstruct the η-values of clusters by matching them to the templates, an average success rate of no more than 50% was observed, despite performing the test using the same sets of clusters as the ones used for the calculation of the templates. In other words, the method performed rather poorly on a test which should be quite easy.

The magnitudes of the standard deviations could most likely be reduced by using more narrow ranges for the calculations, but this would also make the difference between adjacent ranges smaller. Better results could possibly be achieved by being more selective with the clusters used for calculation of the templates, but whether the improvements would be significant enough to make the method viable is doubtful.

Despite the somewhat disappointing results, the work done in this thesis can hopefully provide a basis for further studies of the behavior of the DSSSD detectors. Although the current analysis method gives good results (using proper corrections) for "well behaved" events, it has problems dealing with more problematic ones, such as overlapping hits and clusters containing dead strips. Methods for accurate reconstruction of such events will have to be found before the micro-vertex tracker can reach its full potential.

Bibliography

[1] Krane, K.S., 1988. *Introductory Nuclear Physics*. Hoboken; John Wiley & Sons.

[2] Wamers, F., 2011. *Quasi-free Knockout Reactions with the Proton-dripline Nucleus ^{17}Ne*. Ph.D. Thesis, Technische Universität Darmstadt.

[3] GSI website. `http://www.gsi.de`.

[4] Homepage of the FAIR GmbH.
`http://www.fair-center.org`.

[5] The R3B Collaboration, 2005. *R^3B a universal setup for kinematical complete measurements of reactions with relativistic radioactive nuclei*. Technical proposal, `http://www.gsi.de/forschung/kp/kr/R3B/Technical_Program_e.html`.

[6] The R3B Collaboration, 2009. *Neutron-rich Nuclei at and Beyond the Dripline in the Range Z=4 to Z=10 Studied in Kinematically Complete Measurements of Direct Reactions at Relativistic Energies*. Experiment proposal, GSI.

[7] Kittel, C., 2005. *Introduction to solid state physics*. Hoboken; John Wiley & Sons.

[8] W.R. Leo, 1994. *Techniques for Nuclear and Particle Physics Experiments - A How-to Approach*. Berlin; Springer-Verlag.

[9] Hall, G., 1994. *Semiconductor particle tracking detectors*. Reports on Progress in Physics, 9(3), pp. 481.

[10] Bashindzhagyan, G.L., Korotkova, N.A., 2006. *The Use of Capacitive Charge Division in Silicon Microstrip Detectors*. Instruments and Experimental Techniques, 57(5), pp. 318-330.

[11] Azzarello, P., 2004. *Tests And Production Of The AMS-02 Silicon Tracker Detectors*. Ph.D. Thesis, Université de Genève.

[12] Lechanoine-Leluc, C., on behalf of the AMS Tracker collaboration, 2005. *The AMS-02 Tracker* 29th International Cosmic Ray Conference, 3-11 Aug 2005, Pune, India.

[13] Integrated Infrastructure Initiative for European Nuclear Structure Research (EURONS), 2008. *Joint Research Activity JRA09: Reactions with high-intensity beams of exotic nuclei - Task T-J09-2: High-resolution tracking silicon detectors.* `http://www-win.gsi.de/r3b/RHIB_documents.htm`.

[14] Johansson, H.T., 2010. *Hunting Tools Beyond the Driplines - Performing large-scale nuclear physics experiments.* Ph.D. Thesis, Chalmers University of Technology.

[15] Johansson, H.T., 2007. *The DAQ always runs - Performing large-scale nuclear physics experiments.* Licentiate Thesis, Chalmers University of Technology.

[16] Brun, R. and Rademakers, F., 1997. *Root – an object oriented data analysis framework.* Nuclear Instruments and Methods in Physics Research A, 389, pp. 81-86

[17] Stanoiu, M. et al., 2008. *A novel Si strip array to investigate reaction and decay mechanisms.* Nuclear Instruments and Methods in Physics Research B, 266, pp. 4625-4627.

[18] Alpat, B. et al., 2000. *High-precision tracking and charge selection with silicon strip detectors for relativistic ions.* Nuclear Instruments and Methods in Physics Research A, 446, pp. 522-535.

[19] Johansson, H.T., private communication.

[20] Alpat, B. et al., 2005. *Charge determination of nuclei with the AMS-02 silicon tracker.* Nuclear Instruments and Methods in Physics Research A, 540, pp. 121-130.

[21] Bülling, A. Jansson, L., Jareteg, K., Masgren, R., Risting, G., Shojaee, S., 2010. *Analysis of CALIFA Detector Prototypes and Silicon Strip Detectors.* B.Sc. Thesis, Chalmers University of Technology.

A. Glossary

ADC Amplitude to digital converter. An instrument which converts an analog signal to a numeric value based on its maximum amplitude.

ALADiN A large acceptance dipole magnet. A dipole magnet at the LAND setup which deflects outgoing fragments based on their charges and momenta.

DAQ Data Acquisition. The hardware and software responsible for readout of experiment data.

Dripline The boundaries in the table of nuclides beyond which no bound states exist. The neutron dripline is the limit of nuclear stability with regards to addition of neutrons, running along the lower-right part of the nuclide chart. Analogously, the proton dripline is the limit of nuclear stability when adding protons and runs along the upper-left of the nuclide chart.

DSSSD Double-sided silicon strip detector. See SSD.

Cluster A set of adjacent strips which have collected the charge released by one or multiple particle hits.

Event The passing of an ion through the experimental setup.

FAIR Facility for antiproton and ion research. A planned expansion of the current GSI facility.

FEE Front end electronics. The electronics responsible for amplifying and shaping of detector signals before digitisation.

FRS Fragment separator. A part of the GSI facility which can be used to select specific ions in the secondary beam for further transmission to the experimental caves.

GSI Gesellschaft für Schwerionenforschung. A heavy ion research facility in Darmstadt, Germany.

LAND Large area neutron detector. May refer both to the neutron detector itself, as well as to the experimental setup at GSI where it is located.

R^{3}B Reactions with relativistic radioactive beams. The planned replacement for the LAND-setup as GSI is expanded into FAIR.

SIDEREM Silicon detector readout module. A module designed for readout of the DSSSD detectors at the LAND setup.

SIS Schwerionensynchrotron. The synchrotron at GSI.

SSD Silicon strip detector. A silicon-based detector for energy loss and position measurements. May be single- or double-sided, allowing for position measurement along one or two axes, respectively.

SSSSD Single-sided silicon strip detector. See SSD.

Stretch A segment of data from the *siderem01* unpacker containing one, or several nearby, clusters.

Super-FRS The planned replacement for the FRS as GSI transforms into FAIR.

Trigger A logical signal used to activate the data acquisition for an event.

XB Short for crystal ball. A calorimeter for γ-photons and protons surrounding the beam target at the land setup.